


Precursor Nuclearity and Ligand Effects in Atomically-Dispersed Heterogeneous Iron Catalysts for Alkyne Semi-Hydrogenation

Journal Article

Author(s):

Faust Akl, Dario ; Ruiz-Ferrando, Andrea; Fako, Edvin; Hauert, Roland; Safonova, Olga V.; Mitchell, Sharon; López, Núria; Pérez-Ramírez, Javier

Publication date:

2021-07-21

Permanent link:

<https://doi.org/https://doi.org/10.3929/ethz-b-000493460>

Rights / license:

[In Copyright - Non-Commercial Use Permitted](#)

Originally published in:

ChemCatChem 13(14), <https://doi.org/10.1002/cctc.202100235>

Precursor Nuclearity and Ligand Effects in Atomically-Dispersed Heterogeneous Iron Catalysts for Alkyne Semi-Hydrogenation

Dario Faust Akl,^[a] Andrea Ruiz-Ferrando,^[b] Edwin Fako,^[b] Roland Hauert,^[c] Olga Safonova,^[d] Sharon Mitchell,^{*[a]} Núria López^{*[b]} and Javier Pérez-Ramírez^{*[a]}

- [a] D. Faust Akl, Dr. S. Mitchell, Prof. Dr. Pérez-Ramírez
Institute of Chemical and Bioengineering
Department of Chemistry and Applied Biosciences, ETH Zurich
Vladimir-Prelog-Weg 1, 8093 Zurich (Switzerland)
E-mail: msharon@chem.ethz.ch, jpr@chem.ethz.ch
- [b] A. Ruiz-Ferrando, E. Fako, Prof. N. López
Institute of Chemical Research of Catalonia (ICIQ)
The Barcelona Institute of Science and Technology
Av. Països Catalans 16, 43007 Tarragona (Spain)
E-mail: nlopez@iciq.es
- [c] Dr. R. Hauert
Empa–Swiss Federal Laboratories for Materials Science and Technology
Überlandstrasse 129, 8600 Dübendorf (Switzerland)
- [d] Dr. O. V. Safonova
Paul Scherrer Institute
Forschungsstrasse 111, 5232 Villigen (Switzerland)

Supporting information for this article is given at the end of the document.

Abstract Nanostructuring earth-abundant metals as single atoms or clusters of controlled size on suitable carriers opens new routes to develop high-performing heterogeneous catalysts, but resolving speciation trends remains challenging. Here, we investigate the potential of low-nuclearity iron catalysts in the continuous liquid-phase semi-hydrogenation of various alkynes. The activity depends on multiple factors, including the nuclearity and ligand sphere of the metal precursor and their evolution upon interaction with the mesoporous graphitic carbon nitride scaffold. Density functional theory predicts the favorable adsorption of the metal precursors on the scaffold without altering the nuclearity and preserving some ligands. Contrary to previous observations for palladium catalysts, single atoms of iron exhibit higher activity than larger clusters. Atomistic simulations suggest a central role of residual carbonyl species in permitting low-energy paths over these isolated metal centers.

Introduction

Fine chemicals production relies on palladium-based catalysts for the semi-hydrogenation of alkyne building blocks.^[1] The poor utilization of the precious metal and the presence of hazardous lead in commercially applied Lindlar catalysts drives the search for alternatives such as ultra-dilute palladium-copper alloys,^[2] selective palladium sulfide phases,^[3] or supported nickel-copper alloys.^[4] Iron complexes are known to be active homogeneous catalysts in various selective hydrogenation reactions. Chirik and coworkers demonstrated that tridentate pyridinediimine complexes could achieve turnover frequencies comparable to precious metal catalysts in reducing substituted olefins.^[5] Parallel developments focusing on tridentate phosphinoborate complexes highlighted the need for polydentate ligands to stabilize unsaturated iron intermediates,^[6] which is a common strategy in homogeneous catalysis using earth-abundant metals.^[7] Both approaches involved the use of dinitrogen- or hydride-based pre-catalysts.

The remarkable selectivity of homogeneous iron hydrogenation catalysts^[8] prompted the investigation of heterogeneous counterparts. Colloidal metallic nanoparticles prepared by reducing iron salts with organolithium or Grignard reagents or thermal decomposition of labile complexes could efficiently catalyze the full hydrogenation of a broad range of alkynes and olefins to the respective alkanes.^[9] *In situ* X-ray absorption spectroscopy and deconvolution of light-element scattering contributions in the extended X-ray absorption fine structure (EXAFS) evidenced the difficulty to retain surface reduced phases of iron by identifying a metallic iron core and surface-coordinated solvent molecules.^[9c] Following the same trends, nanoparticle surface passivation by exposure to oxygen was found detrimental to activity,^[10] but protected the metallic core from further oxidation by water or air,^[11] as did embedding the nanoparticles in hydrophobic polymers or ionic liquids.^[12] Indeed, in a comparative study of different silica-supported iron species for phenylacetylene semi-hydrogenation, activity decreased in the order $\text{Fe}^0 > \text{Fe}^{2+} > \text{Fe}^{3+}$ while preserving similar selectivity.^[13] Interestingly, purely iron oxide-based systems were found to enhance the reduction of nitroarenes to anilines.^[14] Comparison of distinct unsupported iron oxides showed that the formation of oxygen vacancies promotes hydrogen activation at adjacent metal centers.^[15] For the same transformation, interfacial FeN_x species originating from high-temperature annealing of iron oxide composites with nitrogen-doped carbon correlated with the catalytic activity.^[16] The creation of planar metal oxide ensembles on reducible supports such as zirconia or titania yielded high selectivity in acetylene semi-hydrogenation. Isotopic marker experiments showed that neighboring hydroxyl groups on the support could adsorb the alkyne and facilitate heterolytic splitting of hydrogen over the iron moieties.^[17] The study of similar catalyst architectures with uniform speciation revealed that Fe^{3+} is the active cation.^[18] Single-atom catalysts (SACs) attract attention for catalytic hydrogenations due to the potential to improve precious metal utilization.^[19] Nevertheless, higher barriers for hydrogen activation and stronger substrate

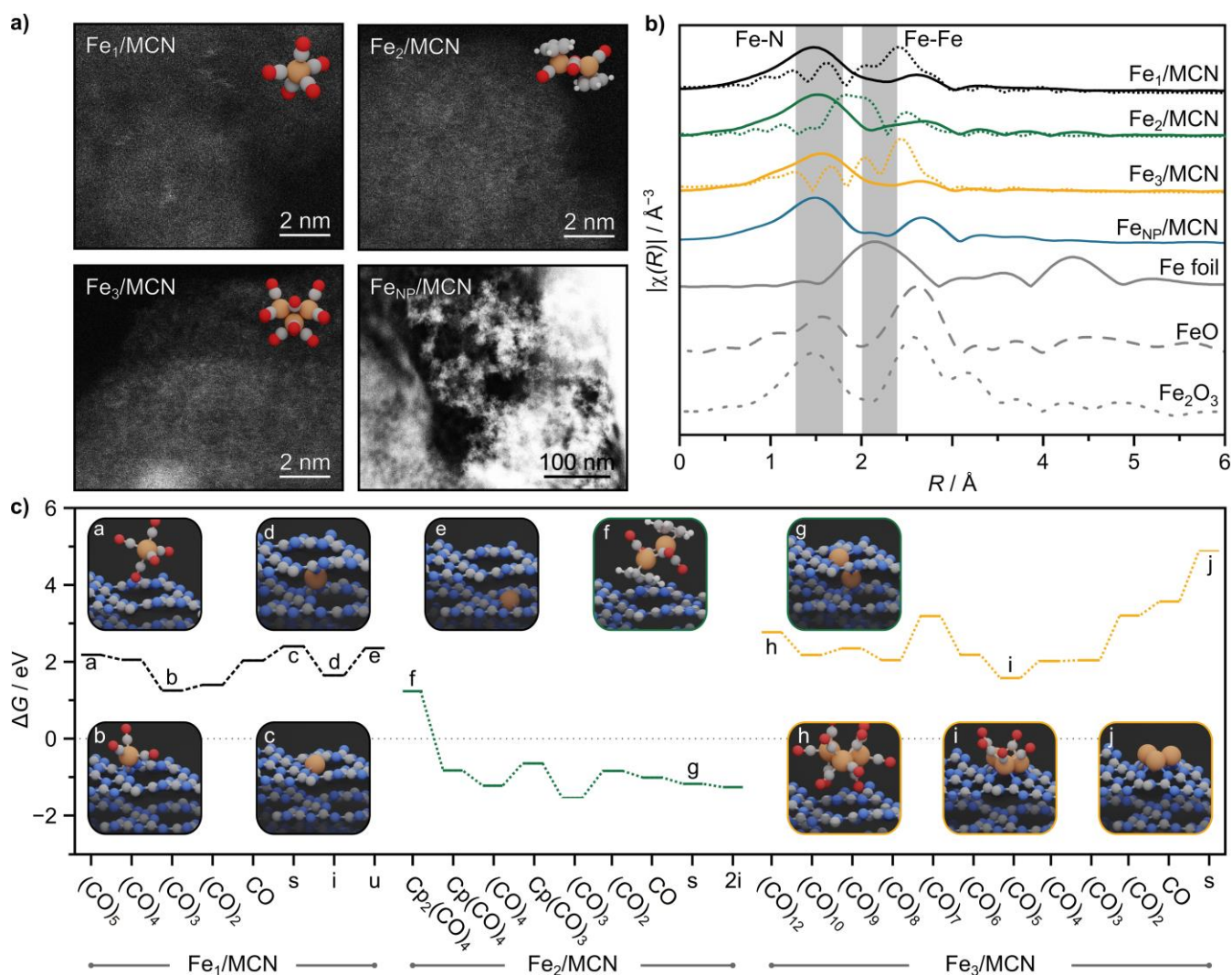


Figure 1. a) AC-ADF-STEM images of Fe_n/MCN catalysts. Insets depict the molecular structure of the employed iron precursors. b) k^2 -weighted Fourier transform of the experimental (solid) and simulated (dotted) EXAFS spectra of Fe_n/MCN , and Fe, FeO, and Fe_2O_3 reference materials. Gray boxes highlight the ranges, where Fe-N/O and Fe-Fe contributions are expected. c) Gibbs energy profiles ($T = 573$ K) describing the successive removal of CO and cyclopentadienyl (Cp) ligands of the deposited iron complexes in the preparation of Fe_n/MCN catalysts with respect to an empty MCN cavity and the isolated precursor (reference state, gray dotted line). Ligand-free iron ensembles are modeled to occupy sites on the surface (s), the interlayer (i), or under the surface (u) of the MCN cavity. Selected calculated structures are depicted as insets. Color code for all panels: Fe-orange; N-blue; C-gray; O-red; H-white.

adsorption render Pd, Rh, or Ir SACs less active than catalysts integrating larger metal ensembles.^[20] On the other hand, earth-abundant metals exhibit intrinsically different speciation trends due to their propensity to stabilize non-metallic phases.^[21] Therefore, it remains to be seen if similar nuclearity features will govern activity trends. The main challenge in elucidating nuclearity effects is the limited atomic-level control of most synthesis techniques. A surface organometallic chemistry approach to prepare silica-grafted dimeric complexes revealed a superior activity for the complete hydrogenation of olefins compared to monomers. However, bulky mesitylene ligands complexed to the metal sites could have altered the 3D local environment significantly.^[22]

Aiming to gain further insight into iron-based alkyne semi-hydrogenation catalysts, we explore the behavior of supported clusters (atoms, dimers, and trimers) on a mesoporous form of graphitic carbon nitride (MCN). The deposition follows a versatile strategy, based on the use of commercially available iron precursors.^[23] Characterization by AC-ADF-STEM and EXAFS

shows that the iron species are atomically-dispersed in all cases while molecular-level simulations evidence favorable adsorption of the iron precursors with partial retention of the ligand sphere. The catalytic evaluation shows that iron is among the few reported metals, where single atoms yield higher metal-specific rates than larger metal species in part due to the different degree of removal of the ligands.

Results and Discussion

Graphitic carbon nitride possesses abundant anchoring sites that stabilize single metal atoms of different elements. Modifications of the carrier morphology to increase the specific surface area can enhance metal dispersion and accessibility. Here, a mesoporous form of graphitic carbon nitride (mesoporous carbon nitride MCN), synthesized *via* a hard-templating approach, was used as a carrier. Elemental analysis

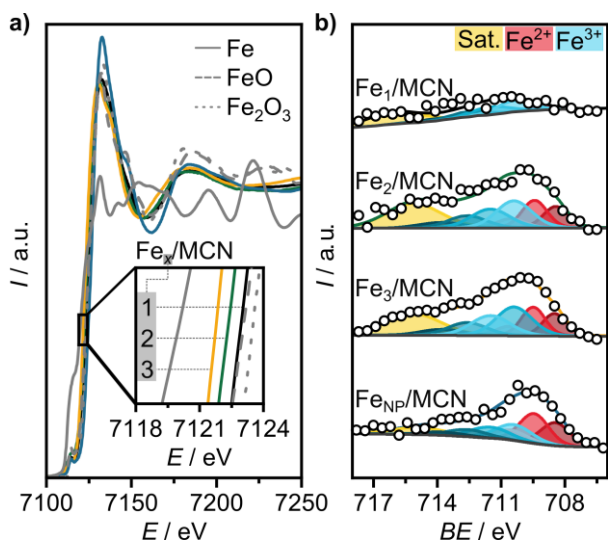


Figure 2. a) Fe K-edge X-ray absorption spectra of the Fe_x/MCN catalysts and Fe, FeO, and Fe_2O_3 references. b) Fe $2p_{3/2}$ photoelectron spectra of the Fe_x/MCN catalysts. Raw data (open circles) and individual components (shaded areas) indicating the assignments of distinct Fe species.

of the resulting material ($\text{C}_3\text{N}_{5.8}\text{O}_{0.8}\text{H}_{0.02}$) reveals slight deviations from the expected composition of graphitic carbon nitride (C_3N_4), with an excess of nitrogen stemming from unpolymerized nitrile groups. Oxygen and hydrogen, present in minor amounts as OH or NH_x functionalities, are partly formed during polymerization or de-templating steps.^[24] Powder X-ray diffraction analysis (XRD) reveals characteristic reflections from long-range stacking of graphitic sheets and reduced crystallinity compared to bulk forms of graphitic carbon nitride (**Figure S1a**).^[25] Nitrogen isotherms (**Figure S1**), secondary electron microscopy (SEM), and transmission electron microscopy (TEM, **Figure S2**) confirm the (meso)porous nature of the MCN (**Figure S1**). Further descriptors of porosity resemble results of previously reported MCN,^[24] with a significantly higher specific surface area ($210 \text{ m}^2 \text{ g}^{-1}$) originating from the ball-milling procedure to mix the precursors preceding thermal polymerization. Assessment of the N $1s$ X-ray photoelectron spectra (XPS) evidences uniform speciation across all materials. Fitted contributions, assigned to tertiary and ring nitrogen functionalities, are characteristic of the tris-triazine units of the carrier (**Figure S3**). The O $1s$ spectra contain features corresponding to C=O and C-O groups and adsorbed water ($\text{H}_2\text{O}_{\text{ads}}$), with total surface oxygen contents ranging between 1 and 4 wt.% (**Figure S3**).

Based on a procedure reporting the deposition of iron dimers on graphitic carbon nitride,^[23] mono- (iron pentacarbonyl), di- (cyclopentadienyl iron dicarbonyl dimer), and trinuclear (triiron dodecacarbonyl) iron complexes with similar ligands were supported on MCN in a DMF solution and subjected to thermal treatment under flowing nitrogen at 573 K. The obtained materials are named Fe_x/MCN , where x indicates the iron precursor nuclearity. Small variations in metal content ($\pm 0.2 \text{ wt.}\%$) compared to the target value (0.5 wt.%) arise because of the specific deposition procedure (**Table 1**). Aberration-corrected annular dark-field scanning transmission electron microscopy (AC-ADF-STEM) confirms the absence of aggregates over the Fe_x/MCN catalysts (**Figure 1a**). However, the nuclearity of the iron species derived from different precursors cannot be distinguished from the images. The low mass contrast between iron and carbon nitride

and the irregular morphology of the carrier add to known challenges of accurate cluster visualization.^[23b] A reference sample containing supported Fe nanoparticles (denoted $\text{Fe}_{\text{NP}}/\text{MCN}$) was obtained by annealing the Fe-containing carrier in. The particles are visualized in the form of larger aggregates (**Figure 1a**), which are clearly identified by energy-dispersive X-ray spectroscopy (EDX, **Figure S4d**). EDX further reveals the elemental uniformity of the materials and the homogenous distribution of iron across the carrier (**Figure S4**).

Analysis of the Fourier transformed EXAFS signal provides insight into the local environment of the supported metal species (**Figure 1b**). The Fe-N(O) scattering paths (1.5 \AA) comprise the major contribution in all materials, coinciding with the consistent presence of isolated iron centers in the nitrogen-containing MCN cavity. The similarity between oxidic references (FeO, Fe_2O_3) and the $\text{Fe}_{\text{NP}}/\text{MCN}$ sample indicate the prevalence of oxidic metal nanoparticles. A metallic Fe-Fe contribution (2.1 \AA) in this material is visible as a small shoulder, but is absent in the Fe_x/MCN catalysts.

Density functional theory (DFT) simulations were conducted to provide further insight into the evolution of the supported iron precursors in the Fe_x/MCN catalysts. Starting from the mono- and multinuclear complexes ($\text{Fe}(\text{CO})_5$, $(\text{C}_5\text{H}_5)_2\text{Fe}_2(\text{CO})_4$, and $\text{Fe}_3(\text{CO})_{12}$) and an empty MCN cavity and gas-phase CO as reference states, the binding Gibbs free energies of successive ligand removal steps at the annealing temperature (573 K) were obtained (**Figure 1c**).

The results reveal appreciable thermodynamic penalties for the removal of carbonyl groups, suggesting that in Fe_1/MCN the iron atom is likely stabilized in the form of $\text{Fe}(\text{CO})_3$. Changes in the coordination environment of Fe atoms due to the loss of two CO ligands strengthen their interaction with the scaffold, leading to a core-level shift of 0.75 eV compared to the physisorbed complex (**Table S1**). A similar scenario is found for the Fe_2/MCN catalyst, where upon cyclopentadienyl ligand removal, the resting complex is $\text{Fe}_2(\text{CO})_3$. For the trimeric complex, the removal of all the CO ligands presents a high energetic cost and is unlikely to proceed to completion ($>3 \text{ eV}$). In effect, partially CO-ligated intermediates such as $\text{Fe}_3(\text{CO})_5$ with a core-level shift of $\sim 1 \text{ eV}$ with respect to Fe-i are likely stabilized. Similar observations were previously made for systems based on clusters of Pt and Rh.^[26]

Thermogravimetric analysis of the iron precursors indicates virtually complete removal of the ligands at the annealing temperature (573 K), as expected from literature values.^[27] Only for the dimeric complex, a second decomposition feature above that temperature corresponding to ca. 5 wt% associated with CO_2 and H_2O formation is observed. Although complete decomposition of the pentacarbonyl precursor is anticipated,

Table 1. Sample notation, iron precursor applied, bulk and surface metal contents, and percentage of Fe^{3+} .

Catalyst	Fe precursor	$W_{\text{Fe,bulk}}^{[a]}$ [wt.%]	$W_{\text{Fe,surface}}^{[b]}$ [wt.%]	$\text{Fe}^{3+[c]}$ [%]
Fe_1/MCN	$\text{Fe}(\text{CO})_5$	0.3	0.16	90
Fe_2/MCN	$(\text{C}_5\text{H}_5)_2\text{Fe}_2(\text{CO})_4$	0.5	0.43	62
Fe_3/MCN	$\text{Fe}_3(\text{CO})_{12}$	0.4	0.40	64
$\text{Fe}_{\text{NP}}/\text{MCN}$	$\text{Fe}(\text{NO}_3)_3 \cdot 9\text{H}_2\text{O}$	0.7	0.47	44

[a] From ICP-OES. [b] From XPS. [c] Estimated from XPS.

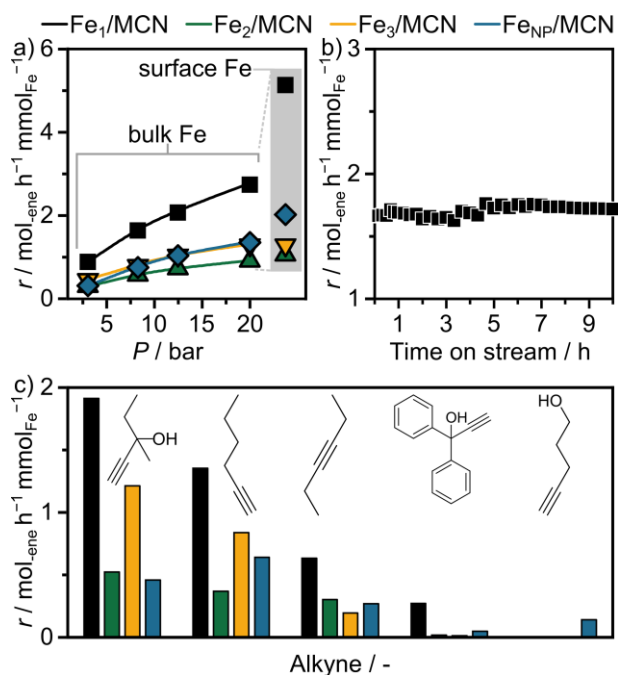


Figure 3. **a)** Rate of 2-methyl-3-buten-2-ol formation as a function of pressure ($T = 323 \text{ K}$) in the flow semi-hydrogenation of MBY. The corresponding rates based on the surface iron concentration are as shown in the gray box ($P = 20 \text{ bar}$). **b)** The rate of alkene formation during the flow semihydrogenation of MBY ($P = 8 \text{ bar}$ and $T = 323 \text{ K}$) over the single-atom catalyst Fe₁/MCN remains stable over 10 h on stream. **c)** Rates of alkene formation in the hydrogenation of various substituted alkynes ($P = 8 \text{ bar}$ and $T = 323 \text{ K}$) over the Fe_{*x*}/MCN catalysts. The legend colors apply to all panels.

minor features in the expected infrared region of diffuse-reflectance infrared spectroscopy (DRIFTS) of the as-prepared Fe₁/MCN catalyst point towards a small fraction of residual CO (Figure S5). The large background absorption assigned to unpolymerized surface groups of the MCN carrier, however makes accurate quantification challenging.

The stabilizing effect of the Fe-O bond on Cp and CO removal was exemplarily investigated by including oxygen defects in the scaffold models of the dimeric species. The surface oxygen abundance evidenced by XPS was represented by replacing a N vacancy in the MCN cavity with a carbonyl functionality. For comparison, Gibbs free energies of the dimeric iron complex were reevaluated on the modified anchoring site, revealing an overall enhanced stabilization through the Fe-O bond (Figure S6). Despite this observation, the general shape of the energy profile of the supported iron dimer is essentially retained. Dissociation into bare Fe-s seems thermodynamically favored, lowering the stability of Fe₂-s as active ensemble. Therefore, the presence of oxygen does not appear to impact the formation of potentially active free coordination sites in such systems. The computational results indicate that the complete removal of ligands leading to bare Fe ensembles as active surface species, either in the form of single atom, dimers, or trimers (Fe-s, Fe₂-s, Fe₃-s, insets c, g, j Figure 1c) is unlikely. Even in instances, where the barriers for surface ensemble formation are low (Fe₁/MCN and Fe₂/MCN), this configuration is furthermore compromised in terms of stability, due to the thermodynamic tendency for the metal to percolate to inactive interlayer positions (Fe-i, inset d Figure 1c).^[28] The surface iron content determined through XPS reveals metal depletion over the single-atom

catalyst (0.1 wt.%) with respect to bulk contents and is therefore in agreement with DFT results. Samples from cluster precursors, and with nanoparticles, in turn, show smaller differences between bulk and surface iron concentration (0.4–0.47 wt.%) (Table 1).

The diversity of iron species over the corresponding Fe_{*x*}/MCN catalysts (Figure 1c) can be rationalized through the relative populations (Boltzmann distribution, Table S2) over the considered intermediates formed through the successive ligand removal steps. This representation of each of the states at the thermodynamic equilibrium depends on the temperature and the Gibbs energy of each intermediate (Table S1). Removed ligands were transferred to gas-phase reservoirs and conformational contributions of the adsorbed organometallic were not taken into account (Computational Methods).

Apart from the most stable tricarbonyl species, the Fe₁/MCN is composed of largely Fe₁(CO)₂/MCN (25.9 %) and Fe-i (15.6 %). In the dimeric instance, a significant share of the metal occupies interlayer positions (Fe-i, 16.4 %), followed by Fe₂(Cp)(CO)₃/MCN (14.9 %) as the third most abundant state. The surface of the Fe₃/MCN catalyst is populated by species bound with 5, 4 and 3 carbonyl ligands in decreasing order, displaying the direct impact of the energetic penalty associated with ligand abstraction (Table S2).

EXAFS spectra for each structure in the formation of the Fe_{*x*}/MCN catalyst were weighted with the Boltzmann populations, yielding representative spectra (Figure 1b). Consistent with experiments revealing the cationic nature of Fe, predominant Fe-O(N) (ca. 1.7 Å) and Fe-O-Fe (2.7 Å) scattering features are observed. However, small shifts with respect to experiments become noticeable at upper radial distances. The precise determination of the coordination sphere through the analysis of EXAFS remains problematic because C, N, and O have similar scattering paths. Analysis of the X-ray absorption near-edge structure (XANES) corroborates the strong interaction leading to a positive charge of the iron (Figure 2a). The whiteline positions close to both oxide reference materials (FeO, Fe₂O₃), are consistent with the cationic (Fe²⁺, Fe³⁺) nature of iron for the Fe_{*x*}/MCN catalysts. Next to the Fe³⁺ reference (7123.5 eV), Fe₁/MCN possesses the highest content of Fe³⁺ and therefore a higher averaged oxidation state than the supported dimers and trimers. Their whiteline is found at lower energies (Figure 2a, inset). The surface iron species identified by the spectral fitting of the Fe_{3*p*3/2} XPS, are exclusively cationic (Fe²⁺ and Fe³⁺), in agreement with the XAS results (Figure 2b).^[29] Threefold positively charged species make out a share of 90 % of the total peak area in Fe₁/MCN, which decreases to around 60 % for Fe₂/MCN and Fe₃/MCN (Table 1). The average oxidation state shifts to a certain extent with precursor nuclearity, which is in agreement with XANES and the magnitude of core-level shifts simulated with DFT (Table S1). Notable differences in signal intensity can be partly ascribed to variations in metal content.

All catalysts were first evaluated in the semi-hydrogenation of the vitamin building block 2-methyl-3-butyn-2-ol (MBY)^[30] in flow. The reaction rate increases with the temperature (Figure S7) and pressure (Figure 3a), but the higher activity does not significantly alter the selectivity to the desired 2-methyl-3-buten-2-ol product (>88 % at 48 % conversion). The main side reaction observed is the over-hydrogenation to 2-methyl-3-butan-2-ol. Increasing the substrate or hydrogen flow rates have the expected effects, resulting in an overall

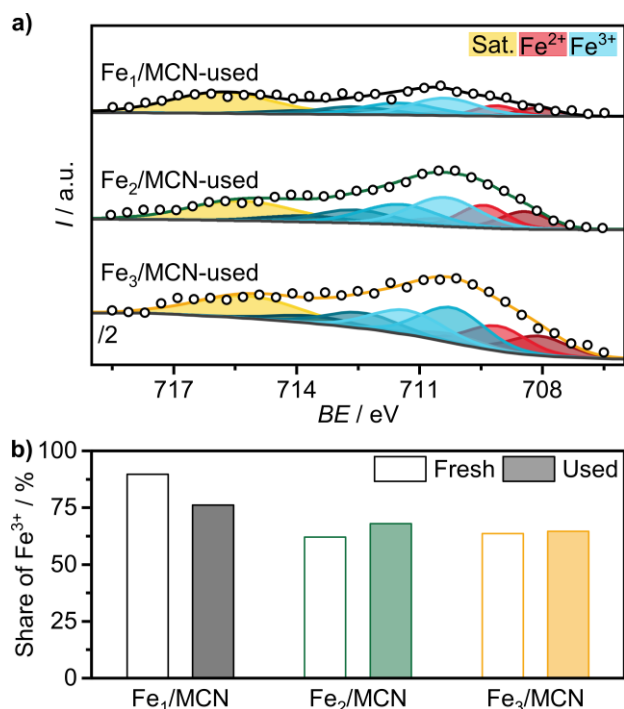


Figure 4. a) Fe $2p_{3/2}$ photoelectron spectra of the used Fe_n /MCN catalysts (circles) and individual components (shaded areas) indicating the assignments of distinct Fe species. b) Share of Fe^{3+} in fresh and used Fe_n /MCN catalysts.

improvement of the activity (Figure S7). In both cases, the catalysts retain a high alkene selectivity. The Fe_2 /MCN catalysts alkene formation rate improves at high substrate concentrations when compared to the rate at standard conditions (ca. 25 % improvement). However, in absolute terms, the single atom catalyst persistently outperforms the other studied materials across all substrate concentrations.

Contrary to palladium and most other precious metals,^[20c, 23b] Fe_1 /MCN consistently outperforms the catalysts derived from dimeric and trimeric complexes throughout the pressure range of 3 to 20 bar in terms of metal-specific rate (Figure 3a). When considering the effective surface metal loading, the single-atom catalyst displays a three times higher reaction rate. Therefore, iron is one of few metals,^[31] for which reducing the nuclearity to 1 enhances reactivity in the selective hydrogenation of acetylenic bonds. Evaluation of the single-atom catalyst stability for 10 h on stream in MBY hydrogenation confirmed its stable performance (Figure 3b). In the transformation of other related alkynes, Fe_1 /MCN again displays superior activity. Here, the detrimental formation of interlayer species from supported iron dimers becomes apparent. Effects of steric hindrance become visible, in converting the less accessible triple bond in 3-hexyne compared to 1-hexyne, resulting in reduced activity. Comparing branched substrates, replacing the methyl substituents in MBY by phenyl groups significantly hinders conversion, while the ethyl group in 1-methyl-3-pentyn-1-ol only has a marginal impact on reactivity. Notably, 4-pentyn-1-ol remains unconverted on the low nuclearity materials. As reported in a previous study of Au-SACs,^[27] the superior reactivity of some alkynols compared to the aliphatic alkynes can result from a directing effect of the hydroxyl group. Consistent with the stable performance in flow semi-hydrogenation, no aggregate formation is visible in ADF-STEM images of the used catalysts and the elemental distribution

remains uniform (Figure S8). Exposure to hydrogenation conditions affects the metal oxidation state only slightly, resulting in a minor reduction in the share of Fe^{3+} in XPS (Figure 4), which could relate to changes in the ligand sphere (*vide infra*).

For the Fe_1 /MCN and Fe_3 /MCN catalysts, DFT simulations of acetylene semi-hydrogenation at reaction temperature ($T = 323$ K), provide further molecular-level insights into the observed activity and selectivity patterns (Figure 5). Since the structures of reaction intermediates of supported iron dimers and trimers are alike and the presence of residual ligands impacts both similarly, the Fe_2 /MCN catalyst was omitted from the following analysis. The reaction profiles for the different reaction networks (Tables S3 and S4) considered both (i) the potential coexistence of different coordination environments in the clusters and (ii) the distinct configurations of adsorbed H_2 and C_2H_2 . Starting from CO (gas), H_2 (gas), C_2H_2 (gas) and the bare ensembles as the reference states, catalysts with and without CO ligands were studied under semi-hydrogenation conditions. $Fe(CO)_3$ /MCN and $Fe_3(CO)_3$ /MCN catalysts were chosen as active ensembles as a compromise between (i) the stability of the ensemble (which determines their relative abundance) and (ii) its potential catalytic activity (in terms of availability of empty coordination sites). The latter is of particular importance in the case of the trimer, since the active site needs to accommodate C_2H_2 and H_2 by forming bridged configurations, which are notably hindered by the presence of CO ligands. Despite $Fe_3(CO)_5$ being the most representative structure of Fe_3 /MCN in terms of stability, $Fe_3(CO)_3$ is expected to exhibit better catalytic performance due to improved substrate adsorption. Consequently, this system is chosen as the active ensemble despite its relatively low expected concentration when compared to the system of choice in Fe_1 /MCN. The reaction starts with the coordination of H_2 to the Fe ensemble to give the dihydrogen complex (H_2^*), which potentially dissociates ($2H^*$) if the accommodation of the H atoms is spatially allowed. Two potential hydrogen dissociation paths are conceivable: (i) heterolytic dissociation, where the MCN lattice acts as a reservoir of protons in a process controlled by electrostatic interactions, and (ii) homolytic dissociation, in which both hydrides adsorb on the same Fe site with a bond angle of 90° .^[32] In Fe_1 /MCN, H_2 dissociates heterolytically, forming a tertiary NH center in the scaffold and a hydride on the Fe atom, which results in a filled coordination sphere of the metal center. As previously proposed, such heterolytic H_2 splitting could occur on other N-doped carbon systems promoted by the basicity of the cavity^[33] and particularly in other single-atom systems on MCN.^[23b] Acetylene adsorption on this complex partially compensates for the energetic cost of the required CO cleavage (~ 0.5 eV at experimental conditions), leading to a hexacoordinated structure of the Fe ensemble ($C_2H_2^*$). The main product then forms by a two-step process consisting of the insertion of the hydride coming from the Fe coordination sphere in the C_2H_2 molecule ($C_2H_3^*$), and the subsequent incorporation of the H from the scaffold on the C_2H_3 motif ($C_2H_4^*$). This step is favorable due to the high stability of the C_2H_4 moiety (Table S3). In Fe_3 /MCN, the presence of three Fe atoms coordinated to the heptazinic N hinders the transfer of H atoms to the host. As observed for trimeric ensembles of palladium on MCN,^[23b] H_2 adsorption by single electron transfer (homolytic dissociation) is favorable over Fe trimers. However, the formation of two hydrides in the presence of three carbonyl ligands would imply

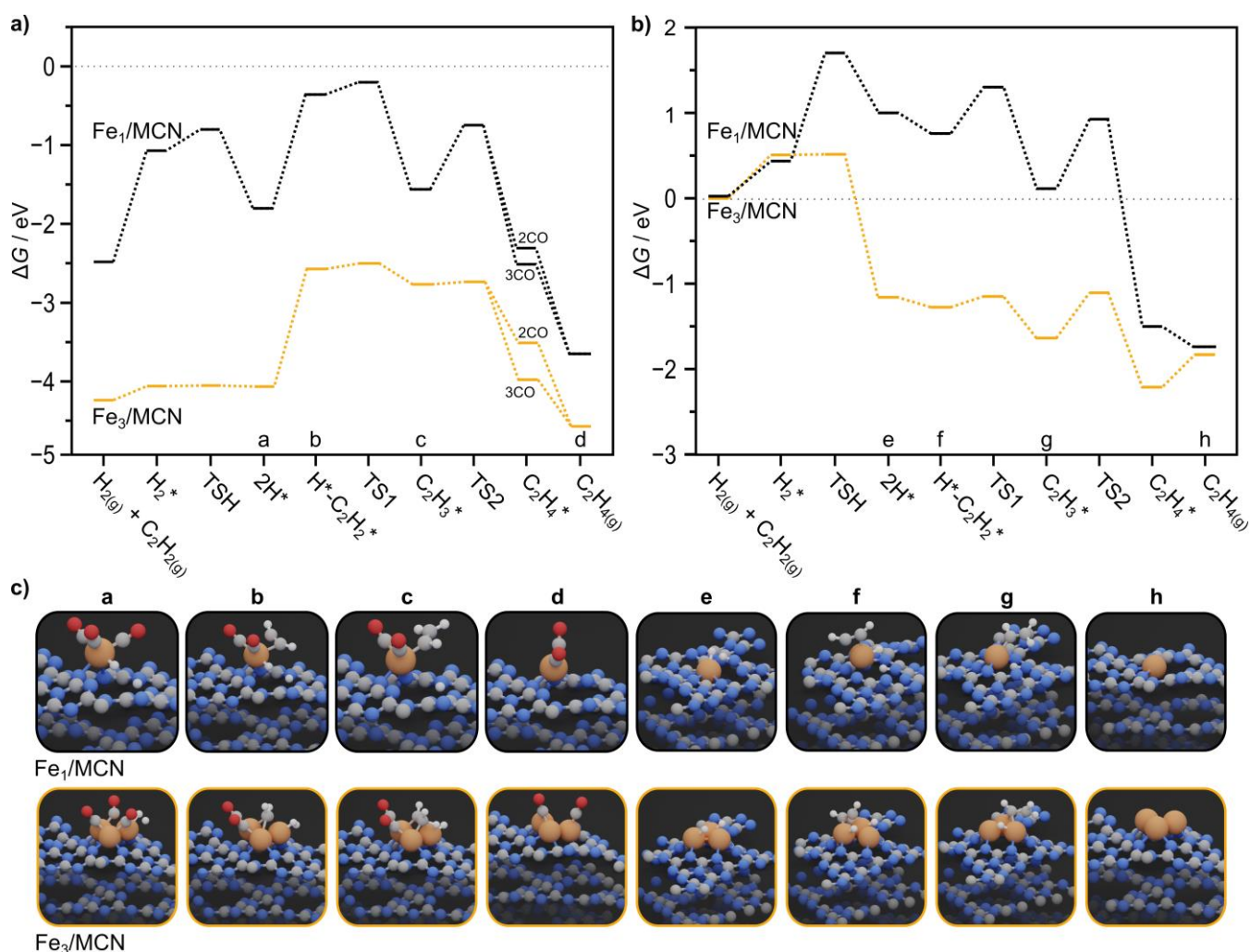


Figure 5. Gibbs energy profiles ($T = 323$ K) of the semi-hydrogenation of acetylene on **a**) CO-containing and **b**) CO-free iron single atoms (Fe_1/MCN) and trimers (Fe_3/MCN). TS denotes transition state. The labels on top of the penultimate intermediate in **a**) correspond to the number of CO ligands bound to the iron site. **c**) Structural models of key intermediates on CO-containing and naked iron catalysts corresponding to the states in **a**) and **b**). Color code for all panels: Fe-brown; N-blue; C-gray; O-red; H-white.

their energetically unfavorable (>1 eV) rearrangement into a terminal configuration. Thus, acetylene directly adsorbs on the molecular hydrogen complex, and the formation of a bridged species with C_2H_2 coordinated to 2 Fe atoms partially compensates the energetic cost of releasing a CO ligand (~ 1.5 eV), which is much higher than for Fe_1/MCN . The alkene is formed more favorably than over the single-atom system.

Although the reaction path over ligand-free systems is virtually the same, significant barriers to form the bare ensembles from thermodynamically favored configurations ($\text{Fe}(\text{CO})_3$ and $\text{Fe}_3(\text{CO})_5$) have to be overcome (~ 2.5 eV for Fe_1/MCN and ~ 5 eV for Fe_3/MCN at 323 K). The highly activated C_2H_4^* moieties on Fe-s and Fe_3 -s potentially could potentially indicate poor chemoselectivity of ligand-free configurations. Investigation of the paths for the full hydrogenation of acetylene to ethane shows that the desorption of the alkene is preferred over the complete hydrogenation in the CO-containing systems, because of the associated penalties of incorporating H into C_2H_4^* and C_2H_5^* . The slightly favored stabilization of C_2H_5^* on trimeric ensembles (Fe_3 -s and $\text{Fe}_3(\text{CO})_2$) compared to single-atom species is caused by the bridging configuration. Hence, the reaction barriers for the

complete hydrogenation are lowered, diminishing the chemoselectivity (**Figure S8**).

Overall, the observed speciation and catalytic performance patterns are akin to CO-containing reaction paths. Importantly, carbonyl ligands ensure the stability of active configurations of iron single atoms by preventing the percolation of iron into the host scaffold, reflected in the respective Boltzmann populations. Concurrently, the thermodynamic penalty associated with carbonyl removal and the dynamic configurations of remaining ligands limit the reactant adsorption on the metal trimers, further reducing the share of active sites. Consequently, iron trimers exhibit low activity despite presenting reduced activation barriers for the semi-hydrogenation of acetylene. In the dimeric instance, the energetically favored formation of interlayer species results in inhibited activity.

Although ligand-free clusters are predicted to be unstable on graphitic carbon nitride, the investigation of ultra-small ensembles of iron on less-interacting carriers could be potentially promising,^[18] as the present analysis of reaction paths shows. Furthermore, the beneficial effect of CO on the single atom catalyst could be of practical relevance for impure industrial

hydrogen feeds and thus alleviate poor CO tolerance of benchmark palladium catalysts.^[34]

The catalytic performance of the Fe_x/MCN catalysts in the alkyne semi-hydrogenation reaction is the complex outcome depending on multiple factors including the scaffold nature, the metal center and nuclearity, and its immediate coordination environment, which relies on the presence of ligands, thus putting non-noble single-atom reactivity even closer to that of homogeneous organometallic catalysts.

Conclusion

The downsizing of iron to low-nuclearity species was investigated as an avenue to nanostructuring earth-abundant metal catalysts for the selective hydrogenation of alkynes. The controlled wet deposition of mono, di, or trimeric carbonyl-based complexes led to highly dispersed metal species with distinct oxidation states in the Fe_x/MCN catalysts. Although it was not possible to directly confirm, DFT simulations supported the preserved nuclearity of metal species following stabilization of the complexes on the host scaffold. In a rare example, the single-atom catalyst outperformed larger metal ensembles in the liquid-phase semi-hydrogenation of various substituted alkynes. Despite the favorable hydrogen activation path over metal trimers, analysis of Boltzmann-distributed populations revealed a higher proportion of unsaturated metal centers in materials containing single atoms than dimers and trimers. This is because of the energetic cost of ligand abstraction to expose the bare metal was significantly higher for the trimeric ensembles. In the case of iron dimers redispersion into single atoms in the interlayer of the carbon nitride scaffold was preferred. This result highlights the importance of analyzing multiple factors when describing the performance of non-noble atomically-disperse catalysts, where ligand, metal center(s), and scaffold are brought together with behavior that is closer to that of homogeneous catalysts. The findings further highlight the need for improved characterization techniques able to discriminate catalytically active environments in detail and consideration of the atomic-scale evolution in the design of low-nuclearity metal catalysts.

Experimental Section

Catalyst Synthesis

Mesoporous graphitic carbon nitride (MCN) was prepared using a hard-templating approach reported elsewhere.^[24] Cyanamide (20 g, 99 %, Sigma Aldrich) was dissolved in colloidal silica (50 g, 40 wt% in water, Ludox HS-40, Sigma Aldrich). After evaporation of the water under stirring at 363 K, the white powder was subjected to ball-milling for 15 min (500 rpm, 3 min resting time between intervals). The ground powder was transferred to crucibles, covered, and heated to 873 K (ramp 2.3 K min⁻¹) for 4 h in a static nitrogen atmosphere. The silica template was removed by treatment in a stirred solution of ammonium hydrogen fluoride (4 M, 40 cm³ g⁻¹SiO₂, Alfa Aesar) for 48 h. The resulting MCN powder was collected by filtration, washed with water followed by ethanol, and dried at 338 K. Iron pentacarbonyl (99.99 %, Sigma Aldrich), cyclopentadienyliron dicarbonyl dimer (99 %, Fluka), and triiron dodecacarbonyl (99 %, Acros) were used as iron precursors without further purification. In a typical procedure, 500 mg of MCN was dispersed in 10 cm³ of N,N-dimethylformamide (99.5 %, Sigma Aldrich) and sonicated for 10 min. The

metal precursor was dissolved in 15 cm³ of solvent and slowly added to the MCN dispersion targeting an iron loading of 0.5 wt.%. The samples are denoted Fe_x/MCN with the precursor nuclearity indicated as a subscript. After stirring overnight, the resulting materials were filtered, washed with ethanol, and dried at 338 K. Finally, the dry powders were thermally annealed at 573 K (ramp 2.3 K min⁻¹) for 5 h in nitrogen flow (20 cm³ min⁻¹) resulting in samples denoted Fe_x/MCN, where *x* = 1-3 reflecting the nuclearity of the iron precursor. Following the procedure, a reference sample containing oxide nanoparticles (denominated Fe_{NP}/MCN) was prepared using iron nitrate nonahydrate (99 %, Sigma Aldrich) as the iron source, deionized water as the solvent, and changing the atmosphere to static air.

Catalyst Characterization

Elemental analysis of C, H, N, and O of the carbon nitride supports was performed in a LECO CHN-900 combustion furnace with an infrared spectrometer. Powder X-ray diffraction (XRD) was performed in a PANalytical X'Pert PRO-MPD instrument. The diffractometer employs a Bragg-Brentano geometry and Ni-filtered Cu K α radiation. Data were collected over a 2 θ range of 3-60° with a step size of 0.08° and a counting time of 163 s per step. The surface area was determined *via* N₂ sorption at 77 K in a Micromeritics TriStar instrument. The samples were degassed at 423 K for around 6 h prior to measurement. The total surface area was determined using the Brunauer-Emmett-Teller (BET) method. X-ray photoelectron spectroscopy (XPS) was carried out in a Physical Electronics Instruments Quantum 2000 instrument with monochromatic Al K α radiation. The beam was operated at 15 kV and 32.3 W. Spectral acquisition occurred under ultrahigh vacuum conditions with a pass energy of 46.95 eV. All spectra were calibrated by the N 1s signal of ring nitrogen at 398.7 eV and fitted with mixed Gaussian-Lorentzian components after Shirley background subtraction. Main and satellite peaks corresponding to Fe²⁺ and Fe³⁺ were narrowly constrained to 710.2 \pm 0.2 eV (Fe³⁺), 708.3 \pm 0.2 eV (Fe²⁺), and 714.5 \pm 1.25 eV (Fe²⁺ satellite). Additional components (Fe³⁺, three, and Fe²⁺, two) were constrained in dependence of the main peak.^[29, 35] The share of Fe³⁺-components from the total fitted area is used as a measure of the average oxidation state. Thermogravimetric analysis was carried out in a Linseis STA PT 1600 instrument using an alumina crucible. The sample (ca. 20 mg) was dried (373 K, 1 h) in an Ar atmosphere (300 cm³ min⁻¹) and heated to 1273 K (ramp 5 K min⁻¹). On-line effluent analysis of likely gaseous products (H₂O, CO, and CO₂) was conducted using a mass spectrometer (MS, Pfeiffer Vacuum ThermoStar GSD T1). For mass loss calculations, removal of all non-iron components of the precursors is assumed. Diffuse-reflectance infrared spectroscopy (DRIFTS) measurements were performed in a Harricks DRIFT cell and a Bruker Optics Vertex 70 spectrometer with a liquid nitrogen-cooled mercury cadmium telluride (MCT) detector. The catalyst was loaded and pressed to obtain a flat surface and degassed at 423 K under Ar flow (30 cm³ min⁻¹) for 1 h. Finally, the spectrum was acquired at 303 K. KBr was used for measurement of the background signal. The metal content determination was performed *via* inductively coupled plasma optical emission spectroscopy (ICP-OES) in a Horiba Ultra 2 instrument (photomultiplier tube detector). The solid (approximately 5 mg) was loaded in a polytetrafluoroethylene tube containing an HNO₃:H₂O₂ mixture (3:1, 2 cm³). Subsequently, the tubes were heated to 533 K *via* microwave irradiation under autogenous pressure for 20 min. Following digestion, the obtained clear solutions were diluted to 25 cm³ with Millipore water and filtered before analysis. High-angle annular dark field-scanning transmission electron microscopy (ADF-STEM) and energy-dispersive X-ray spectroscopy (EDX) elemental maps were measured in a Talos F200X instrument with a FEI SuperX detector at 200 kV acceleration potential. The catalysts were dusted on standard copper or nickel mesh holey carbon films (EMresolutions). Aberration-corrected (AC)-ADF-STEM measurements were performed on an HD2700-CS Hitachi microscope with beam diameters of 0.1 and 0.2 nm equipped with secondary-electron and energy dispersive X-ray detectors. Image frame times ranged from 20 to 40 μ s (1024x1024 pixel). X-ray absorption spectroscopy (XAS) was conducted at the X10DA (SuperXAS) beamline of the Swiss Light Source.

The X-ray beam from the 2.9 T superbend was collimated using a Si-coated mirror, monochromatized using a Si(111) channel-cut monochromator, and focused to a spot size of 500×100 μm (horizontal×vertical) using a Rh-coated toroidal mirror. Data were acquired from pressed pellets at the Fe Kedge in transmission mode, using three 15 cm long Ar/N₂-filled ionization chambers. The samples were placed between the first and the second ionization chamber. For the absolute energy calibration, an Fe foil was measured simultaneously between the second and a third ionization chambers. The resulting spectra were energy-calibrated, background-corrected, and normalized using the Athena program from the Demeter software suite.

Catalyst Evaluation

Continuous flow hydrogenation experiments were performed in a ThalesNano H-Cube Pro setup. The catalyst was pressed and sieved (mesh size 200–400 μm) and 100 mg of the fraction was loaded in a stainless-steel cartridge (3.5 mm internal diameter). The remaining volume was filled with silicon carbide (46 grit, Alfa Aesar). A 0.4 M reaction solution of 2-methyl-3-butyn-2-ol (MBY, 98 %, Sigma Aldrich) in toluene (99.8 %, Fischer Scientific) was continuously fed with a rate of $F_L = 1 \text{ cm}^3 \text{ min}^{-1}$ and mixed with *in situ* generated hydrogen ($F_G = 36 \text{ cm}^3 \text{ min}^{-1}$) before contact with the catalyst cartridge. The standard conditions employed were $P = 8 \text{ bar}$ and $T = 323 \text{ K}$, with an equilibration time under steady conditions of 10 min prior to sample collection. To explore the substrate scope, the semi-hydrogenation of 1-hexyne (98 %, Acros), 3-hexyne (99 %, Acros), 4-pentyn-1-ol (97 %, Sigma Aldrich), 3-methyl-1-pentyn-3-ol (98 %, TCI), or 1,1-diphenyl-2-propyn-1-ol (99 %, Sigma Aldrich) in toluene (0.4 M) were also studied. The obtained liquid product was analyzed offline with a gas chromatograph (HP-6890, HP-5 capillary column) equipped with a flame ionization detector (FID). The metal-specific rate of alkene formation r was used as a comparative measure and is quantified from the liquid flowrate (F_L), the feed concentration (c_0), the conversion (X), the alkene selectivity (S_{ene}), and the bulk ($n_{\text{Fe,bulk}}$) and surface amounts of iron ($n_{\text{Fe,surf}}$). Unconverted alkyne (c_{yne}) and over-hydrogenated alkane (c_{ane}) of the corresponding substrate are considered for the selectivity calculation. These metrics are computed using equations (1-3).

$$X = \frac{c_0 - c_{\text{yne}}}{c_0} \quad (1)$$

$$S_{\text{ene}} = \frac{c_{\text{ene}}}{c_{\text{ene}} + c_{\text{ane}}} \quad (2)$$

$$r = \frac{c_0 F_L X S_{\text{ene}}}{n_{\text{Fe,bulk}}} \quad (3)$$

Computational Methods

Spin-polarized density functional theory (DFT) simulations were performed using the Vienna Ab Initio Simulation Package (VASP) code.^[36] A generalized gradient approximation (GGA) was employed, expressed by the Perdew–Burke–Ernzerhof functional^[37] with D3 dispersion correction^[37,38] to describe van der Waals interactions. Inner electrons were described by projector augmented waves (PAW),^[39] while valence electrons were expanded in plane waves with a cut-off kinetic energy of 450 eV. Models for the potential structures formed *in situ* for each set (Fe₁/MCN, Fe₂/MCN, and Fe₃/MCN), the reaction intermediates, and transition states were constructed in a (2x2) heptazinc supercell with four layers of thickness, with the bottom one frozen to the configuration of the bulk. Slabs were separated by 14 Å of vacuum and a dipole correction along the z-direction was used.^[40] The Brillouin zone was sampled with a gamma-centered 3×3×1 *k*-point grid (~0.3 Å). In all cases, the ionic and electronic convergence criteria were 10⁻⁴ and 10⁻⁵ eV, respectively. Transition states were located using the climbing image nudged elastic band algorithm^[41] and confirmed by diagonalizing the numerical Hessian matrix obtained by displacements of ±0.02 Å. Simulated EXAFS spectra were generated using FEFF8^[42] and post-processed with Athena.^[43] All inputs, outputs, and structures can be accessed through the ioChem-BD^[44]

repository using the following link: <https://www.doi.org/10.19061/iochem-bd-1-197>^[45]

To compute the Boltzmann population of each system, ligands are removed to gas-phase reservoirs and conformational contributions of the adsorbed organometallic moieties are not taken into account. The bridge to terminal ligands in Fe₃(CO)_Y (Y = 4-11) gas-phase structures are known to behave dynamically (barrier 0.25 eV for their bridge-opening bridge-closing).^[46] Although ensemble calculations would be ideal for this purpose including all entropic terms,^[47] the scaffold limits the multiplicity of the structures (complicating its evaluation) and their fluxionality due to a wall effect. Thus, only one possible structure for each system was considered. The energy differences when removing ligands are large enough to ensure that the considered resting states are relevant even if these contributions were not introduced in the model.

Acknowledgments

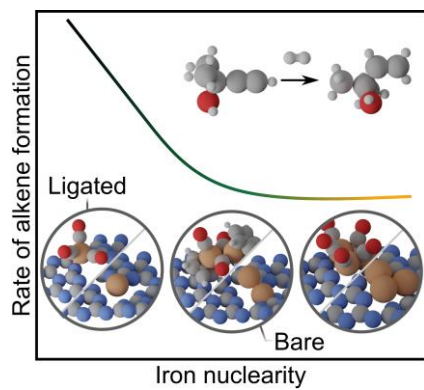
This publication was created as part of NCCR Catalysis, a National Centre of Competence in Research funded by the Swiss National Science Foundation. Dr. Evgeniya Vorobyeva and Dr. Frank Krumeich for assistance with electron microscopy and ScopeM at ETH Zurich for access to their facilities. BSC-RES for providing generous computational resources.

Keywords: Alkyne hydrogenation • Iron catalysts • Nuclearity effects • Single atoms • Carbon nitride

- [1] G. Vilé, D. Albani, N. Almora-Barrios, N. López, J. Pérez-Ramírez, *ChemCatChem* **2016**, *8*, 21-33.
- [2] a) A. J. McCue, A. Gibson, J. A. Anderson, *Chem. Eng. J.* **2016**, *285*, 384-391; b) M. J. Taylor, S. K. Beaumont, M. J. Islam, S. Tsatsos, C. A. M. Parlett, M. A. Issacs, G. Kyriakou, *Appl. Catal. B* **2021**, *284*, 119737.
- [3] a) Y. Liu, Y. Li, J. A. Anderson, J. Feng, A. Guerrero-Ruiz, I. Rodríguez-Ramos, A. J. McCue, D. Li, *J. Catal.* **2020**, *383*, 51-59; b) D. Albani, M. Shahrokhi, Z. Chen, S. Mitchell, R. Hauert, N. López, J. Pérez-Ramírez, *Nat. Commun.* **2018**, *9*, 2634.
- [4] Y. Liu, A. J. McCue, P. Yang, Y. He, L. Zheng, X. Cao, Y. Man, J. Feng, J. A. Anderson, D. Li, *Chem. Sci.* **2019**, *10*, 3556-3566.
- [5] a) S. C. Bart, E. Lobkovsky, P. J. Chirik, *J. Am. Chem. Soc.* **2004**, *126*, 13794-13807; b) R. J. Trovitch, E. Lobkovsky, E. Bill, P. J. Chirik, *Organometallics* **2008**, *27*, 1470-1478.
- [6] K. Junge, K. Schröder, M. Beller, *Chem. Commun.* **2011**, *47*, 4849-4859.
- [7] R. M. Bullock, J. G. Chen, L. Gagliardi, P. J. Chirik, O. K. Farha, C. H. Hendon, C. W. Jones, J. A. Keith, J. Klosin, S. D. Minteer, R. H. Morris, A. T. Radosevich, T. B. Rauchfuss, N. A. Strotman, A. Vojvodic, T. R. Ward, J. Y. Yang, Y. Surendranath, *Science* **2020**, *369*, eabc3183.
- [8] a) P. J. Chirik, *Acc. Chem. Res.* **2015**, *48*, 1687-1695; b) S. Enthaler, K. Junge, M. Beller, *Angew. Chem. Int. Ed.* **2008**, *47*, 3317-3321.
- [9] a) P. H. Phua, L. Lefort, J. A. Boegers, M. Tristany, J. G. de Vries, *Chem. Commun.* **2009**, 3747-3749; b) C. Rangheard, C. de Julian Fernandez, P. H. Phua, J. Hoorn, L. Lefort, J. G. de Vries, *Dalton Trans.* **2010**, *39*, 8464-8471; c) A. Welther, M. Bauer, M. Mayer, A. Jacobi von Wangelin, *ChemCatChem* **2012**, *4*, 1088-1093; d) V. Kelsen, B. Wendt, S. Werkmeister, K. Junge, M. Beller, B. Chaudret, *Chem. Commun.* **2013**, *49*, 3416-3418.
- [10] M. Stein, J. Wieland, P. Steurer, F. Tolle, R. Mülhaupt, B. Breit, *Adv. Synth. Catal.* **2011**, *353*, 523-527.
- [11] R. Hudson, A. Rivière, C. M. Cirtiu, K. L. Luska, A. Moores, *Chem. Commun.* **2012**, *48*, 3360-3362.
- [12] a) T. N. Gieshoff, A. Welther, M. T. Kessler, M. H. Pechtl, A. Jacobi von Wangelin, *Chem. Commun.* **2014**, *50*, 2261-2264; b) R. Hudson, G. Hamasaka, T. Osako, Y. M. A. Yamada, C. J. Li, Y. Uozumi, A. Moores, *Green Chem.* **2013**, *15*, 2141-2148.
- [13] a) A. A. Shesterkina, E. V. Shuvalova, O. A. Kirichenko, L. M. Kustov, *Russ. J. Phys. Chem. A* **2018**, *92*, 2412-2416; b) A. A. Shesterkina, E.

- V. Shuvalova, E. A. Redina, O. A. Kirichenko, O. P. Tkachenko, I. V. Mishin, L. M. Kustov, *Mendeleev Commun.* **2017**, *27*, 512-514.
- [14] a) M. Benz, A. M. van der Kraan, R. Prins, *Appl. Catal. A* **1998**, *172*, 149-157; b) I. T. Papadas, S. Fountoulaki, I. N. Lykakis, G. S. Armatas, *Chem. Eur. J.* **2016**, *22*, 4600-4607.
- [15] H. L. Niu, J. H. Lu, J. J. Song, L. Pan, X. W. Zhang, L. Wang, J. J. Zou, *Ind. Eng. Chem. Res.* **2016**, *55*, 8527-8533.
- [16] a) R. V. Jagadeesh, A. E. Surkus, H. Junge, M. M. Pohl, J. Radnik, J. Rabeah, H. Huan, V. Schunemann, A. Brückner, M. Beller, *Science* **2013**, *342*, 1073-1076; b) R. V. Jagadeesh, K. Natte, H. Junge, M. Beller, *ACS Catal.* **2015**, *5*, 1526-1529; c) B. Sahoo, C. Kreyenschulte, G. Agostini, H. Lund, S. Bachmann, M. Scalone, K. Junge, M. Beller, *Chem. Sci.* **2018**, *9*, 8134-8141; d) Z. J. Wei, Y. X. Hou, X. M. Zhu, L. Y. Guo, Y. X. Liu, A. Y. Zhang, *ChemCatChem* **2018**, *10*, 2009-2013.
- [17] M. Tejada-Serrano, J. R. Cabrero-Antonino, V. Mainar-Ruiz, M. López-Haro, J. C. Hernández-Garrido, J. J. Calvino, A. Leyva-Pérez, A. Corma, *ACS Catal.* **2017**, *7*, 3721-3729.
- [18] M. Tejada-Serrano, M. Mon, B. Ross, F. Gonell, J. Ferrando-Soria, A. Corma, A. Leyva-Pérez, D. Armentano, E. Pardo, *J. Am. Chem. Soc.* **2018**, *140*, 8827-8832.
- [19] a) S. K. Kaiser, Z. Chen, D. Faust Akl, S. Mitchell, J. Pérez-Ramírez, *Chem. Rev.* **2020**, *120*, 11703-11809; b) S. Mitchell, E. Vorobyeva, J. Pérez-Ramírez, *Angew. Chem. Int. Ed.* **2018**, *57*, 15316-15329; c) L. Zhang, M. Zhou, A. Wang, T. Zhang, *Chem. Rev.* **2020**, *120*, 683-733. d) G. Kyriakou, M. B. Boucher, A. D. Jewell, E. A. Lewis, T. J. Lawton, A. E. Baber, H. L. Tierney, M. Flytzani-Stephanopoulos, E. C. Sykes, *Science* **2012**, *335*, 1209-1212.
- [20] a) J. Lu, P. Serna, C. Aydin, N. D. Browning, B. C. Gates, *J. Am. Chem. Soc.* **2011**, *133*, 16186-16195; b) E. Guan, B. C. Gates, *ACS Catal.* **2017**, *8*, 482-487; c) M. Rondelli, G. Zwaschka, M. Krause, M. D. Rötzer, M. N. Hedhili, M. P. Högerl, V. D'Elia, F. F. Schweinberger, J.-M. Basset, U. Heiz, *ACS Catal.* **2017**, *7*, 4152-4162.
- [21] C. Sun, N. Mammen, S. Kaappa, P. Yuan, G. Deng, C. Zhao, J. Yan, S. Malola, K. Honkala, H. Hakkinen, B. K. Teo, N. Zheng, *ACS Nano* **2019**, *13*, 5975-5986.
- [22] R. R. Langeslay, H. Sohn, B. Hu, J. S. Mohar, M. Ferrandon, C. Liu, H. Kim, A. Jeremy Kropf, C. Yang, J. Niklas, O. G. Poluektov, E. Ercan Alp, P. Ignacio-de Leon, A. P. Sattelberger, A. S. Hock, M. Delferro, *Dalton Trans.* **2018**, *47*, 10842-10846.
- [23] a) S. Tian, Q. Fu, W. Chen, Q. Feng, Z. Chen, J. Zhang, W. C. Cheong, R. Yu, L. Gu, J. Dong, J. Luo, C. Chen, Q. Peng, C. Draxl, D. Wang, Y. Li, *Nat. Commun.* **2018**, *9*, 2353; b) E. Vorobyeva, E. Fako, Z. Chen, S. M. Collins, D. Johnstone, P. A. Midgley, R. Hauert, O. V. Safonova, G. Vilé, N. López, S. Mitchell, J. Pérez-Ramírez, *Angew. Chem. Int. Ed.* **2019**, *58*, 8724-8729.
- [24] Z. P. Chen, S. Mitchell, E. Vorobyeva, R. K. Leary, R. Hauert, T. Furnival, Q. M. Ramasse, J. M. Thomas, P. A. Midgley, D. Dontsova, M. Antonietti, S. Pogodin, N. López, J. Pérez-Ramírez, *Adv. Funct. Mater.* **2017**, *27*, 1605785.
- [25] Z. P. Chen, E. Vorobyeva, S. Mitchell, E. Fako, N. López, S. M. Collins, R. K. Leary, P. A. Midgley, R. Hauert, J. Pérez-Ramírez, *Natl. Sci. Rev.* **2018**, *5*, 642-652.
- [26] M. M. Kauppinen, M. M. Melander, K. Honkala, *Catal. Sci. Technol.* **2020**, *10*, 5847-5855.
- [27] a) J. Phillips, B. Clausen, J. A. Dumesic, *J. Phys. Chem.* **1980**, *84*, 1814-1822; b) K. Asakura, K. Ooi, Y. Iwasawa, *J. Mol. Catal.* **1992**, *74*, 345-351; c) T. S. Piper, F. A. Cotton, G. Wilkinson, *J. Inorg. Nucl. Chem.* **1955**, *1*, 165-174.
- [28] E. Vorobyeva, V. C. Gerken, S. Mitchell, A. Sabadell-Rendón, R. Hauert, S. Xi, A. Borgna, D. Klose, S. M. Collins, P. A. Midgley, D. M. Kepaptsoglou, Q. M. Ramasse, A. Ruiz-Ferrando, E. Fako, M. A. Ortuño, N. López, E. M. Carreira, J. Pérez-Ramírez, *ACS Catal.* **2020**, *10*, 11069-11080.
- [29] M. C. Biesinger, B. P. Payne, A. P. Grosvenor, L. W. M. Lau, A. R. Gerson, R. S. C. Smart, *Appl. Surf. Sci.* **2011**, *257*, 2717-2730.
- [30] S. Vernuccio, R. Goy, P. R. von Rohr, J. Medlock, W. Bonrath, *React. Chem. Eng.* **2016**, *1*, 445-453.
- [31] R. Lin, D. Albani, E. Fako, S. K. Kaiser, O. V. Safonova, N. López, J. Pérez-Ramírez, *Angew. Chem. Int. Ed.* **2019**, *58*, 504-509.
- [32] D. Albani, M. Capdevila-Cortada, G. Vilé, S. Mitchell, O. Martin, N. López, J. Pérez-Ramírez, *Angew. Chem. Int. Ed.* **2017**, *129*, 10895-10900.
- [33] J. L. Fiorio, R. V. Gonçalves, E. Teixeira-Neto, M. A. Ortuño, N. López, L. M. Rossi, *ACS Catal.* **2018**, *8*, 3516-3524.
- [34] M. García-Mota, B. Bridier, J. Pérez-Ramírez, N. López, *J. Catal.* **2010**, *273*, 92-102.
- [35] A. P. Grosvenor, B. A. Kobe, M. C. Biesinger, N. S. McIntyre, *Surf. Interface Anal.* **2004**, *36*, 1564-1574.
- [36] a) G. Kresse, J. Furthmüller, *Phys. Rev. B* **1996**, *54*, 11169-11186; b) G. Kresse, J. Furthmüller, *Comput. Mater. Sci.* **1996**, *6*, 15-50.
- [37] J. P. Perdew, K. Burke, M. Ernzerhof, *Phys. Rev. Lett.* **1996**, *77*, 3865-3868.
- [38] S. Grimme, J. Antony, S. Ehrlich, H. Krieg, *J. Chem. Phys.* **2010**, *132*, 154104.
- [39] a) P. E. Blöchl, *Phys. Rev. B* **1994**, *50*, 17953-17979; b) G. Kresse, D. Joubert, *Phys. Rev. B* **1999**, *59*, 1758-1775.
- [40] G. Makov, M. C. Payne, *Phys. Rev. B* **1995**, *51*, 4014-4022.
- [41] G. Henkelman, H. Jónsson, *J. Chem. Phys.* **2000**, *113*, 9978-9985.
- [42] M. Newville, *J. Synchrotron Radiat.* **2001**, *8*, 322-324.
- [43] B. Ravel, M. Newville, *J. Synchrotron Radiat.* **2005**, *12*, 537-541.
- [44] M. Álvarez-Moreno, C. de Graaf, N. López, F. Maseras, J. M. Poblet, C. Bo, *J. Chem. Inf. Model.* **2015**, *55*, 95-103.
- [45] A. Ruiz-Ferrando, ioChem-BD Dataset. DOI: 10.19061/iochem-bd-1-197
- [46] B. E. Mann, *J. Chem. Soc., Dalton Trans.* **1997**, 1457-1472.
- [47] B. Zandkarimi, A. N. Alexandrova, *WIREs Comput. Mol. Sci.* **2019**, *9*, e1420

TOC Figure



Friend or foe? Catalysts prepared by depositing iron carbonyl complexes of distinct nuclearity on graphitic carbon nitride exhibit differing activity in the liquid-phase semi-hydrogenation of alkynes. Simulations reveal that the superior performance of single-atom catalysts originates from the partial retention of carbonyl ligands, which despite introducing a high energetic cost for their removal, ensure the accessibility of the metal center.

Supporting Information

Precursor Nuclearity and Ligand Effects in Atomically-Dispersed Iron Catalysts for Alkyne Semi-Hydrogenation

Dario Faust Akl, Andrea Ruiz-Ferrando, Edvin Fako, Roland Hauert, Olga Safonova, Sharon Mitchell,*
Núria López,* Javier Pérez-Ramírez*

* Corresponding authors. E-mails: msharon@chem.ethz.ch
nlopez@iciq.es
jpr@chem.ethz.ch

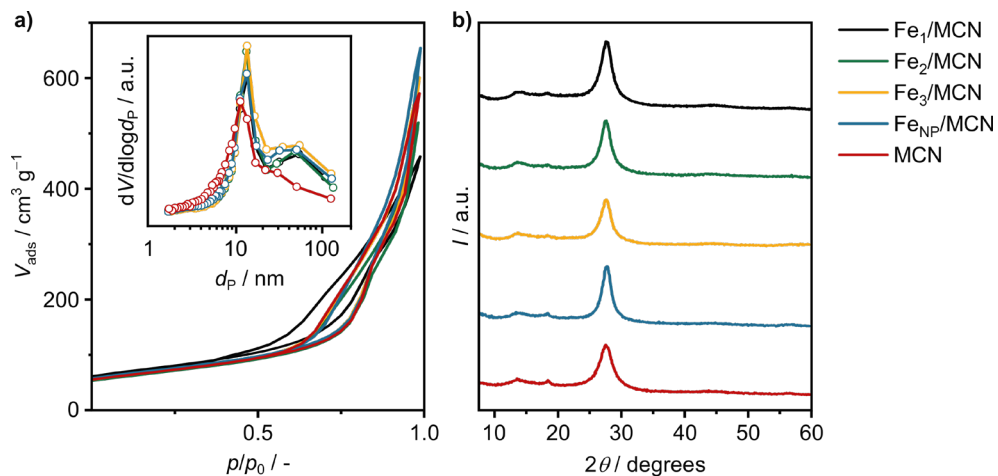


Figure S1. a) Nitrogen isotherms and Barrett-Joyner-Halenda pore size (d_p) distribution (inset) at 77 K of the Fe_x/MCN catalysts and the metal-free carrier (MCN). The total surface area of the solids was in the range of 216-231 $\text{m}^2 \text{g}^{-1}$ and the mesopore size corresponds to the 12 nm-sized template particles. **b)** XRD patterns of the Fe_x/MCN catalysts and MCN. The legend applies to both panels. The samples exhibit showing typical reflections of in-plane repeated motifs and interlayer stacking of graphitic carbon nitride at 13 and 27° 2θ , respectively.^[1] No reflections indicative of the presence of crystalline iron-containing phases were identified.

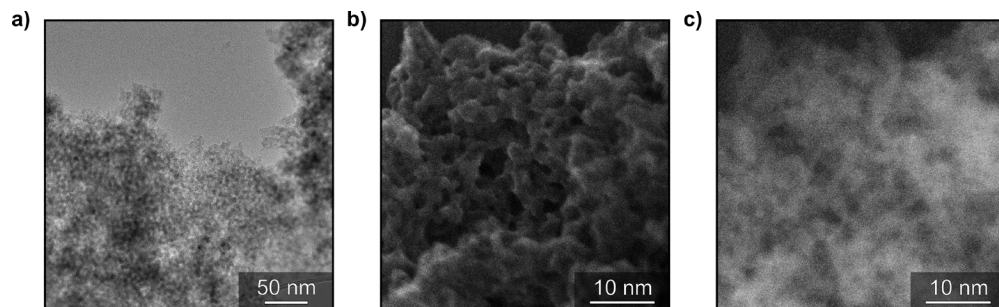
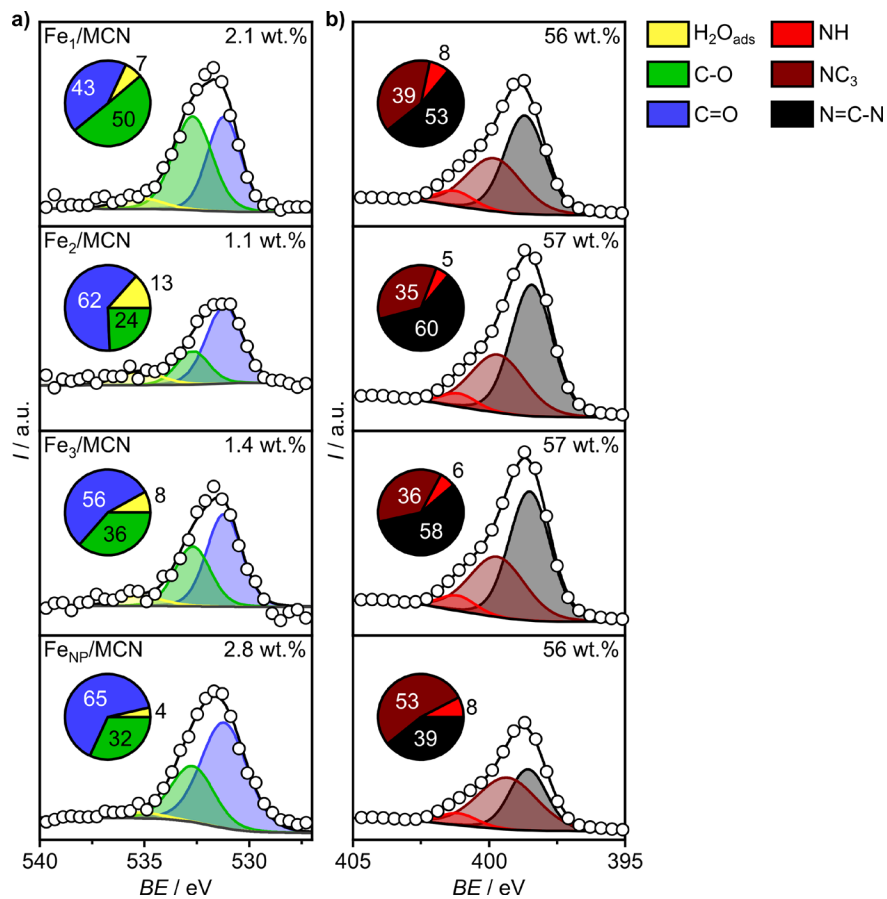


Figure S2. a) TEM, b) SEM, and c) corresponding AC-ADF-STEM images showing the morphology of MCN. Mesopores of varying size are uniformly distributed across the carrier.



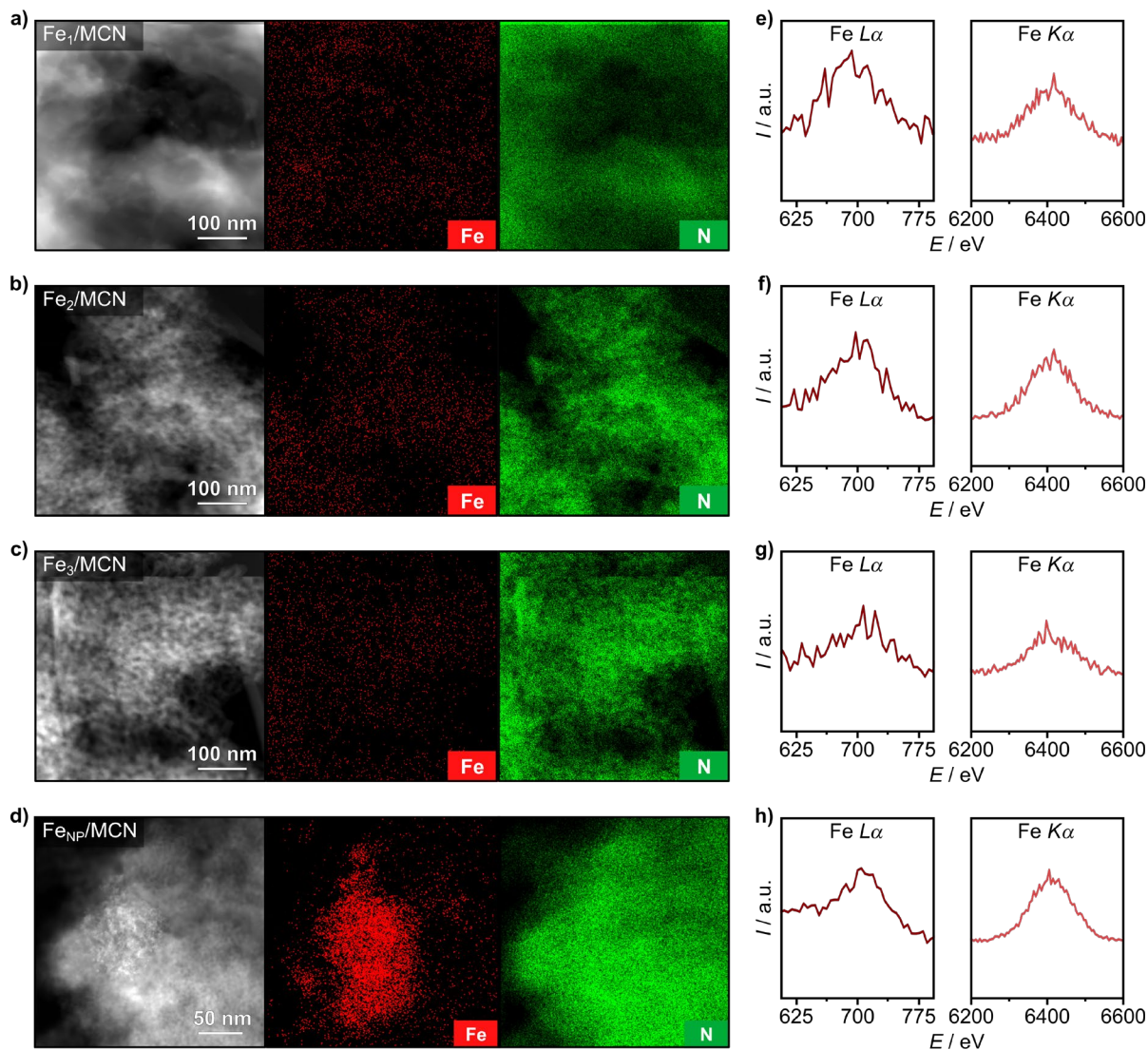


Figure S4. a)-d) ADF-STEM images and corresponding elemental maps of Fe and N of Fe_x/MCN catalysts, revealing a homogeneous distribution of the metal. Localization of the iron signal is evident in Fe_{NP}/MCN consistent with the presence of aggregated nanoparticles in this sample (panel d). e)-h) The main emission lines of iron corroborate the presence of the element in the mapped areas.

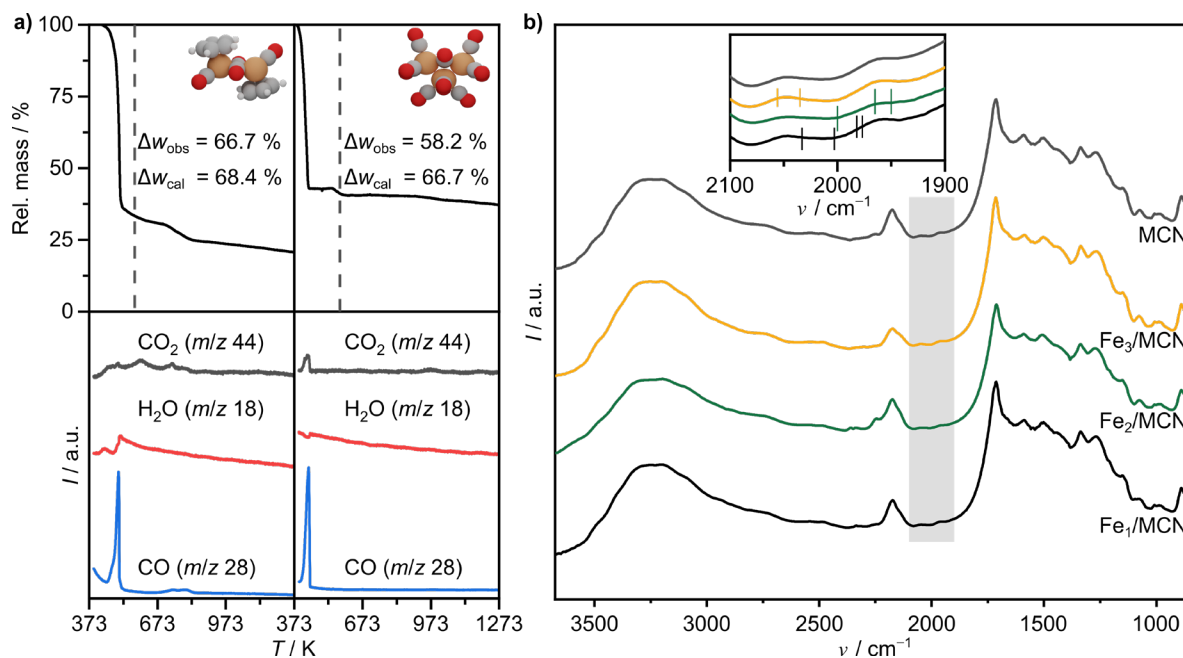


Figure S5. a) Thermogravimetric profiles of the dimeric and trimeric iron precursors (structures shown inset. Color code: Fe-brown; C-gray; O-red; H-white). A sharp decomposition is observed in both cases below the temperature of thermal activation (573 K, dashed lines) coupled to the evolution of CO, CO₂ and H₂O as evidenced by mass spectrometry. The observed weight loss (Δw_{obs}) at 573 K is close to the calculated value (Δw_{cal}), assuming the complete decomposition of the precursors. A significant deviation of 8% for the trimeric precursor arises due to CO loss during the drying step.^[3] **b)** The DRIFT spectra of the catalysts Fe_x/MCN are virtually identical to the one of the MCN carrier. Aside from bands corresponding to the condensed heptazinic rings, defect features (e.g., NH_x- or unpolymerized cyano-groups) are evidenced, coinciding with literature reports.^[2] A zoom of the region defined by the grey box is shown inset, where characteristic CO-vibrations (indicated by vertical lines) of the iron precursors are expected.^[3,4]

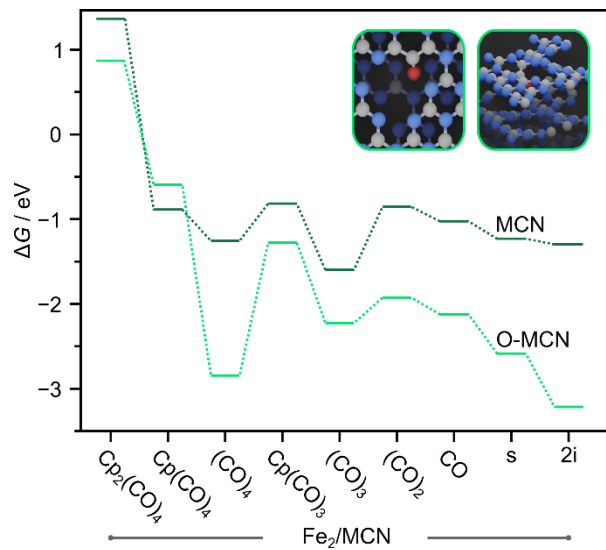


Figure S6. Gibbs energy profiles at $T = 573$ K describing the successive removal of cyclopentadienyl (Cp) and CO ligands of the deposited iron dimeric complexes on the cavities of pristine and O-doped mesoporous carbon nitride. The formation of a ligand-free dimer on a surface position (s) precedes the cleavage into two iron atoms in interlayer position (2i). Color code for the inset: N-blue; C-gray; O-red.

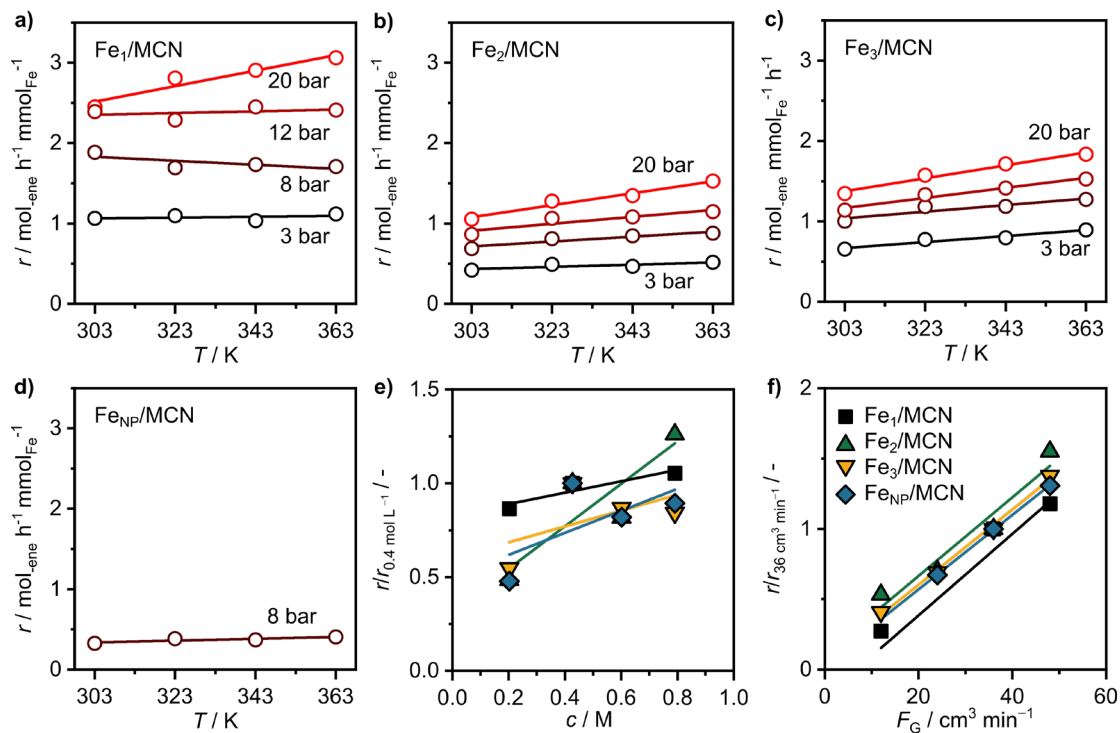


Figure S7. Rate of alkene formation in the flow semi-hydrogenation of 2-methyl-3-butyn-2-ol over Fe_x/MCN catalysts as a function of **a)-d)** temperature and pressure, **e)** inlet alkyne concentration (c , $T = 323 \text{ K}$, $P = 8 \text{ bar}$), and **f)** hydrogen flowrate (F_G , $T = 323 \text{ K}$, $P = 8 \text{ bar}$). The rates in **e)** and **f)** were normalized with respect to standard conditions ($c = 0.4 \text{ M}$, $F_G = 36 \text{ cm}^3 \text{ min}^{-1}$). The legend in **f)** applies to **e)**.

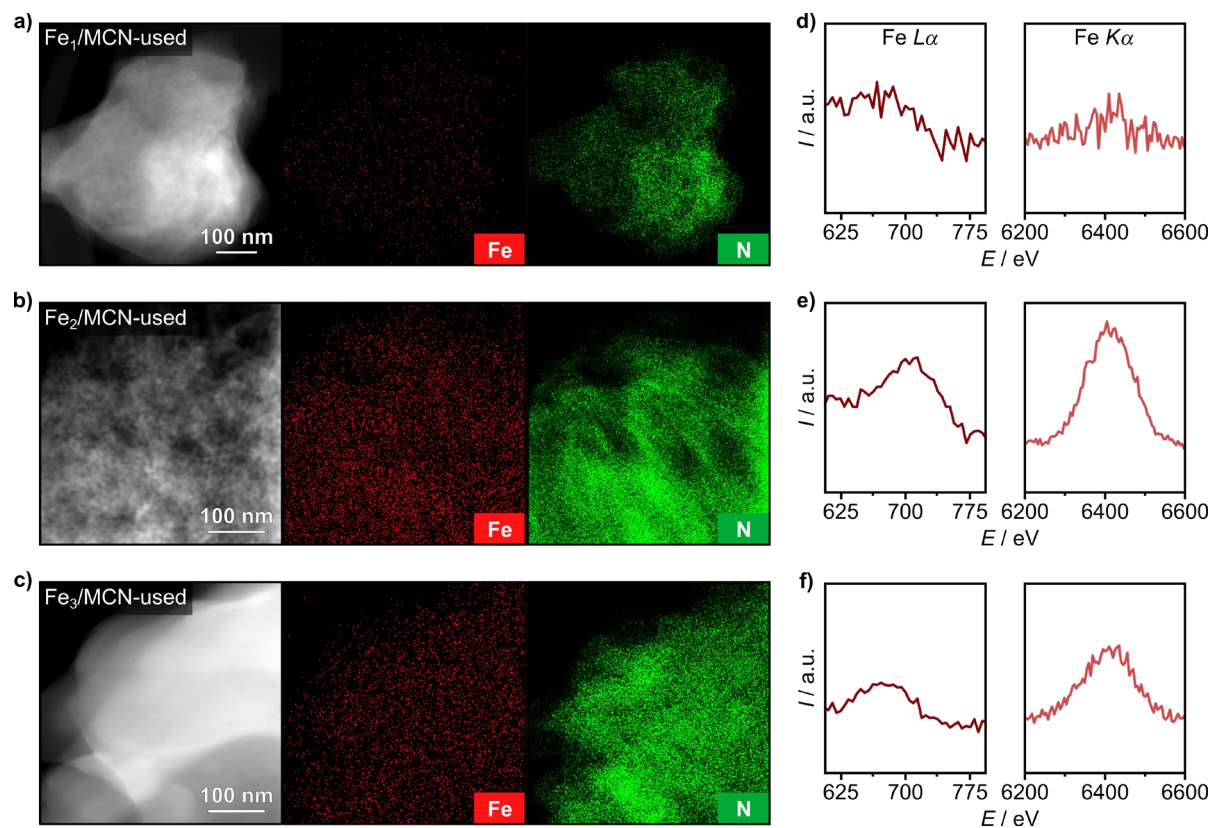


Figure S8. a)-c) ADF-STEM images and corresponding elemental maps of Fe and N in the Fe_x/MCN catalysts recovered after use in the flow semi-hydrogenation of 2-methyl-3-butyn-2-ol ($P = 20$ bar, $T = 363$ K), revealing the preserved atomic dispersion of the metal. **e)-h)** The main emission lines of iron corroborate the presence of the element in the mapped areas.

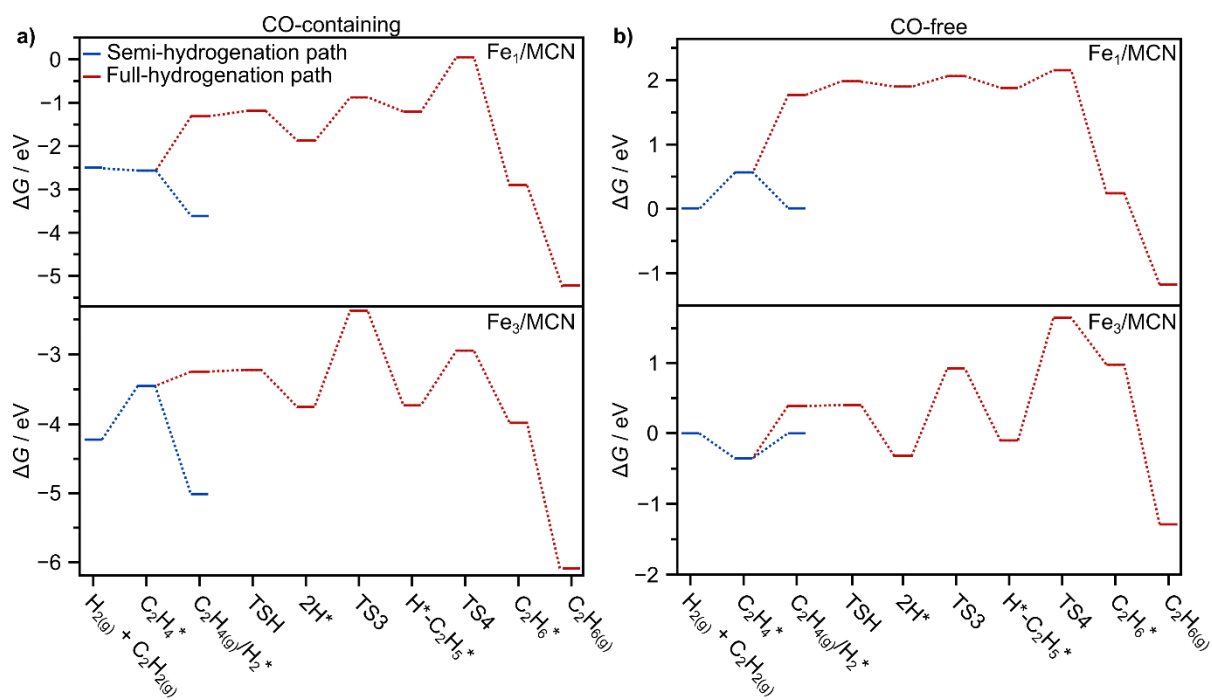


Figure S9. Gibbs energy profiles at $T = 323$ K of semi- and full-hydrogenation paths of acetylene on **a)** CO-containing and **b)** CO-free iron single atoms and trimers. The legend in **a)** applies to **b)**. TS denotes transition state.

Table S1. Simulated Fe 2p core-level shifts and adsorption Gibbs free energies ($T = 573$ K) of the deposited iron complexes in the preparation of Fe_x/MCN catalysts.

Type of ensemble	Structure	$G_{\text{form}}^{[\text{a}]} / \text{eV}$	Relative core level shift		
			1	2	3
Single atom	$\text{Fe}(\text{CO})_5$	2.22	3.22 ^[b]		
	$\text{Fe}(\text{CO})_4$	2.03	2.16		
	$\text{Fe}(\text{CO})_3$	1.33	2.47		
	$\text{Fe}(\text{CO})_2$	1.43	0.53		
	$\text{Fe}(\text{CO})$	2.06	1.18		
	Fe-s	2.47	-0.04		
	Fe-i	1.67	0.00		
	Fe-u	2.38	0.18		
Dimer	$\text{Fe}_2(\text{Cp})_2(\text{CO})_4$	1.37	0.95	0.95	
	$\text{Fe}_2(\text{Cp})(\text{CO})_4$	-0.85	0.18	0.79	
	$\text{Fe}_2(\text{Cp})(\text{CO})_3$	-1.30	0.58	0.17	
	$\text{Fe}_2(\text{CO})_4$	-0.73	0.64	0.98	
	$\text{Fe}_2(\text{CO})_3$	-1.64	0.25	0.81	
	$\text{Fe}_2(\text{CO})_2$	-0.82	0.36	0.14	
	Fe_2CO	-1.04	0.18	-0.16	
	$\text{Fe}_2\text{-s}$	-1.25	-0.27	1.32	
	2 Fe-i	-1.35	0.00		
Trimer	$\text{Fe}_3(\text{CO})_{12}$	2.79	1.90	1.89	2.14
	$\text{Fe}_3(\text{CO})_{10}$	2.23	1.21	1.21	0.53
	$\text{Fe}_3(\text{CO})_9$	2.42	1.23	1.28	0.56
	$\text{Fe}_3(\text{CO})_8$	2.09	1.25	1.25	0.68
	$\text{Fe}_3(\text{CO})_7$	3.23	0.75	0.72	0.21
	$\text{Fe}_3(\text{CO})_6$	2.24	1.08	0.68	0.66
	$\text{Fe}_3(\text{CO})_5$	1.60	0.10	0.63	0.55
	$\text{Fe}_3(\text{CO})_4$	2.07	0.67	0.78	0.51
	$\text{Fe}_3(\text{CO})_3$	2.09	0.34	0.35	0.34
	$\text{Fe}_3(\text{CO})_2$	3.18	0.77	0.63	0.55
	Fe_3CO	3.74	-0.10	0.21	-0.06
	$\text{Fe}_3\text{-s}$	5.04	-0.21	-0.21	-0.24

^[a] Formation energies are calculated as the difference in Gibbs free energy of the adsorbed ensemble *versus* an empty cavity and the isolated precursor molecule. ^[b] Fe-i was chosen as reference state for Fe core levels as it is the most stable configuration for a ligand-free single atom of Fe.

Table S2. Boltzmann populations of the different structures modelled for Fe₁/MCN, Fe₂/MCN, and Fe₃/MCN as shown in **Figure 1c** and computed from the respective formation energies G_{form} .

Ensemble type	Structure	$P_i^{[a]} / \%$
Single atom	Fe(CO) ₅	5.2
	Fe(CO) ₄	7.7
	Fe(CO) ₃	31.6
	Fe(CO) ₂	25.9
	Fe(CO)	7.12
	Fe-s	3.15
	Fe-i	15.6
	Fe-u	3.7
Dimer	Fe ₂ (Cp) ₂ (CO) ₄	0.1
	Fe ₂ (Cp)(CO) ₄	6.0
	Fe ₂ (Cp)(CO) ₃	14.9
	Fe ₂ (CO) ₄	4.7
	Fe ₂ (CO) ₃	29.9
	Fe ₂ (CO) ₂	5.7
	Fe ₂ CO	8.8
	Fe ₂ -s	13.4
Fe-i	16.4	
Trimer	Fe ₃ (CO) ₁₂	2.9
	Fe ₃ (CO) ₁₀	9.2
	Fe ₃ (CO) ₉	6.2
	Fe ₃ (CO) ₈	12.0
	Fe ₃ (CO) ₇	1.2
	Fe ₃ (CO) ₆	8.9
	Fe ₃ (CO) ₅	33.0
	Fe ₃ (CO) ₄	12.7
	Fe ₃ (CO) ₃	12.1
	Fe ₃ (CO) ₂	1.3
	Fe ₃ CO	0.4
Fe ₃ -s	0.0	

^[a] The relative population P_i is computed with $P_i = \frac{e^{-\beta G_{\text{form},i}}}{\sum_j e^{-\beta G_{\text{form},j}}}$

Table S3. Gibbs barriers and reaction energies (in eV) of the catalyzed semi-hydrogenation on CO-containing ($\text{Fe}(\text{CO})_3$, $\text{Fe}_3(\text{CO})_3$) and CO-free surface iron species (Fe-s, Fe_3 -s) in Fe_1/MCN and Fe_3/MCN catalysts. The system denominations correspond to the structures shown in **Figure 1d**.

System	1 st H ₂		C ₂ H ₃ *		C ₂ H ₄ *		2 nd H ₂		C ₂ H ₅ *		C ₂ H ₆ *	
	addition		formation		formation		addition		formation		formation	
	G_a	ΔG	G_a	ΔG	G_a	ΔG	G_a	ΔG	G_a	ΔG	G_a	ΔG
$\text{Fe}(\text{CO})_3$	0.21	0.71	0.13	-1.17	0.76	-0.95	0.34	1.90	1.04	0.81	1.11	-1.78
$\text{Fe}_3(\text{CO})_3$	0.00	0.23	0.05	-0.22	0.02	-0.76	0.00	0.87	1.28	-0.09	0.80	-0.15
Fe-s	1.33	0.98	0.62	-0.62	0.86	-1.47	0.40	1.99	0.30	-0.13	0.37	-1.68
Fe_3 -s	0.00	-1.08	0.19	-0.41	0.63	-0.50	0.00	-0.29	1.17	0.21	1.66	1.12

Table S4. Imaginary vibrational frequencies (in cm^{-1}) for the transition states on CO-containing ($\text{Fe}(\text{CO})_3$, $\text{Fe}_3(\text{CO})_3$) and CO-free surface iron species (Fe-s, Fe_3 -s) in Fe_1/MCN and Fe_3/MCN catalysts. The systems correspond to the structures shown in **Figure 1d**.

System	1 st H ₂ addition	C ₂ H ₃ * formation	C ₂ H ₄ * formation	2 nd H ₂ addition	C ₂ H ₅ * formation	C ₂ H ₆ * formation
Fe(CO) ₃	1653	697	750	166	419	1177
Fe ₃ (CO) ₃		656	319		940	2133
Fe-s	1251	557	372	1112	400	364
Fe ₃ -s		129	416		793	1051

Supplementary References

- [1] X. Wang, K. Maeda, A. Thomas, K. Takanabe, G. Xin, J. M. Carlsson, K. Domen, M. Antonietti, *Nat. Mater.* **2009**, *8*, 76-80.
- [2] Z. P. Chen, S. Mitchell, E. Vorobyeva, R. K. Leary, R. Hauert, T. Furnival, Q. M. Ramasse, J. M. Thomas, P. A. Midgley, D. Dontsova, M. Antonietti, S. Pogodin, N. López, J. Pérez-Ramírez, *Adv. Funct. Mater.* **2017**, *27*, 1605785.
- [3] K. Asakura, K. Ooi, Y. Iwasawa, *J. Mol. Catal.* **1992**, *74*, 345-351.
- [4] a) F. A. Cotton, H. Stammreich, G. Wilkinson, *J. Inorg. Nucl. Chem.* **1959**, *9*, 3-7; b) R. K. Sheline, K. S. Pitzer, *J. Am. Chem. Soc.* **1950**, *72*, 1107-1112.